Stanford Exploration Project, Report 120, May 3, 2005, pages 23–40

Target-oriented wave-equation inversion

Alejandro A. Valenciano, Biondo Biondi, and Antoine Guitton[1]

ABSTRACT

A target-oriented strategy can be applied to estimate the wave-equation least-squares inverse image ($\hat{\mathbf{m}}$) by explicitly computing the Hessian ($\mathbf{H}$). The least-squares inverse image is obtained as the solution, using a conjugate gradient algorithm, of a non-stationary least-squares filtering problem $\mathbf{H}\hat{\mathbf{m}} = \mathbf{m}_{mig}$ (where $\mathbf{m}_{mig}$ is the migration image, and the rows of the Hessian are non-stationary filters). This approach allows us to perform the number of iterations necessary to achieve the convergence, by exploiting the sparsity and structure of the Hessian matrix. The results on a constant velocity model and a model with a velocity Gaussian anomaly show the validity of the method.

INTRODUCTION

Seismic imaging (migration) operators are non-unitary (Claerbout, 1992) because they depend on: (1) the seismic experiment acquisition geometry (Nemeth et al., 1999; Duquet and Marfurt, 1999; Ronen and Liner, 2000), (2) the complex subsurface geometry (Prucha et al., 2000; Kuehl and Sacchi, 2001), and (3) the bandlimited characteristics of the seismic data (Chavent and Plessix, 1999). Often, they produce images with reflectors correctly positioned but with biased amplitudes.

Attempts to solve this problem have used the power of geophysical inverse theory (Tarantola, 1987), which compensates for the experimental deficiencies (e.g., acquisition geometry, obstacles) by weighting the migration result with the inverse of the Hessian. However, the main difficulty with this approach is the explicit calculation of the Hessian and its inverse.

Since accurate imaging of reflectors is more important at the reservoir level, we propose to compute the Hessian in a target-oriented fashion (Valenciano and Biondi, 2004). This allows us to reduce the Hessian matrix dimensions. We also exploit the sparsity and structure of the Hessian matrix to dramatically reduce the amount of computation while constructing it. After, we compute the least-squares inverse image as the solution of a non-stationary least-squares filtering problem, by means of a conjugate gradient algorithm.

In this paper, we first discuss the structure and sparsity of the target-oriented Hessian. After that, we show how to compute the least-squares inverse image by solving a non-stationary least-squares filtering problem. We illustrate the methodology with two numerical examples,

[1]**email:** valencia@sep.stanford.edu, biondo@sep.stanford.edu, antoine@sep.stanford.edu

the first in a constant velocity model, and the second in a velocity model with a low velocity Gaussian anomaly.

LINEAR LEAST-SQUARES INVERSION

Tarantola (1987) formalizes the geophysical inverse problem by giving a theoretical approach to compensate for the experiment's deficiencies (e.g., acquisition geometry, obstacles), while being consistent with the acquired data. His approach can be summarized as follows: given a linear modeling operator $\mathbf{L}$ to compute synthetic data $\mathbf{d}$,

$$\mathbf{d} = \mathbf{L}\mathbf{m}, \tag{1}$$

where $\mathbf{m}$ is a reflectivity model, and given the recorded data $\mathbf{d}_{obs}$, a quadratic cost function,

$$S(\mathbf{m}) = \|\mathbf{d} - \mathbf{d}_{obs}\|^2 = \|\mathbf{L}\mathbf{m} - \mathbf{d}_{obs}\|^2, \tag{2}$$

is formed. The model of the earth $\hat{\mathbf{m}}$ that minimize $S(\mathbf{m})$ is given by

$$\hat{\mathbf{m}} = (\mathbf{L}'\mathbf{L})^{-1}\mathbf{L}'\mathbf{d}_{obs} \tag{3}$$
$$\hat{\mathbf{m}} = \mathbf{H}^{-1}\mathbf{m}_{mig}, \tag{4}$$

where $\mathbf{L}'$ (migration operator) is the adjoint of the linear modeling operator $\mathbf{L}$, $\mathbf{m}_{mig}$ is the migration image, and $\mathbf{H} = \mathbf{L}'\mathbf{L}$ is the Hessian of $S(\mathbf{m})$.

The main difficulty with this approach is the explicit calculation of the Hessian inverse. In practice, it is more feasible to compute the least-squares inverse image as the solution of the linear system of equations

$$\mathbf{H}\hat{\mathbf{m}} = \mathbf{m}_{mig}, \tag{5}$$

by using an iterative conjugate gradient algorithm.

Another difficulty with this approach is that the explicit calculation of the Hessian for the entire model space is unfeasible in practice. In the next section we discuss a way to overcome this problem.

TARGET-ORIENTED HESSIAN: DIMENSIONS AND STRUCTURE

Since accurate imaging of reflectors is more important in the neighborhood of the reservoir, it makes sense to restrain the model space to the target area. A way to achieve this objective is to write the modeling operator $\mathbf{L}$ in a target-oriented fashion and explicitly compute the Hessian.

Target-oriented Hessian

In general, the synthetic data for one frequency, a shot positioned at $\mathbf{x}_s = (0, x_s, y_s)$ and a receiver positioned at $\mathbf{x}_r = (0, x_r, y_r)$ can be given by a linear operator $\mathbf{L}$ acting on the full model space $\mathbf{m}(\mathbf{x})$ with $\mathbf{x} = (z, x, y)$ ($\mathbf{x} = (z, x)$ in $2D$) as

$$\mathbf{d}(\mathbf{x}_s, \mathbf{x}_r; \omega) = \mathbf{L}\mathbf{m}(\mathbf{x}) = \sum_{\mathbf{x}} \mathbf{G}(\mathbf{x}, \mathbf{x}_s; \omega)\, \mathbf{G}(\mathbf{x}, \mathbf{x}_r; \omega)\, \mathbf{m}(\mathbf{x}), \tag{6}$$

where $\mathbf{G}(\mathbf{x}, \mathbf{x}_s; \omega)$ and $\mathbf{G}(\mathbf{x}, \mathbf{x}_r; \omega)$ are the Green functions from the shot position $\mathbf{x}_s$ and the receiver position $\mathbf{x}_r$ to a point in the model space $\mathbf{x}$, respectively.

In equation (6), we use two important properties (Ehinger et al., 1996): first, the Green functions are computed by means of the one-way wave equation, and second, the extrapolation is performed by using the adequate paraxial wave equations (flux conservation) (Bamberger et al., 1988).

The quadratic cost function is

$$S(\mathbf{m}) = \sum_{\omega} \sum_{\mathbf{x}_s} \sum_{\mathbf{x}_r} \| \mathbf{d} - \mathbf{d}_{obs} \|^2, \tag{7}$$

and its second derivative with respect to the model parameters $\mathbf{m}(\mathbf{x})$ and $\mathbf{m}(\mathbf{y})$ is the Hessian

$$\begin{aligned} \mathbf{H}(\mathbf{x}, \mathbf{y}) &= \frac{\partial^2 S(\mathbf{m})}{\partial \mathbf{m}(\mathbf{x}) \partial \mathbf{m}(\mathbf{y})} \\ \mathbf{H}(\mathbf{x}, \mathbf{y}) &= \sum_{\omega} \sum_{\mathbf{x}_s} \mathbf{G}'(\mathbf{x}, \mathbf{x}_s; \omega) \mathbf{G}(\mathbf{y}, \mathbf{x}_s; \omega) \sum_{\mathbf{x}_r} \mathbf{G}'(\mathbf{x}, \mathbf{x}_r; \omega) \mathbf{G}(\mathbf{y}, \mathbf{x}_r; \omega), \end{aligned} \tag{8}$$

where $\mathbf{G}'(\mathbf{x}, \mathbf{x}_r; \omega)$ is the adjoint of $\mathbf{G}(\mathbf{x}, \mathbf{x}_r; \omega)$.

Notice that computing $\mathbf{H}(\mathbf{x}, \mathbf{y})$ in equation (8) needs only the precomputed Green functions at model points $\mathbf{x}$ and $\mathbf{y}$. Thus, the size of the problem can be considerably reduced by computing the Green functions only at the target location $\mathbf{x}_T$, reducing equation (8) to

$$\mathbf{H}(\mathbf{x}_T, \mathbf{y}_T) = \sum_{\omega} \sum_{\mathbf{x}_s} \mathbf{G}'(\mathbf{x}_T, \mathbf{x}_s; \omega) \mathbf{G}(\mathbf{y}_T, \mathbf{x}_s; \omega) \sum_{\mathbf{x}_r} \mathbf{G}'(\mathbf{x}_T, \mathbf{x}_r; \omega) \mathbf{G}(\mathbf{y}_T, \mathbf{x}_r; \omega). \tag{9}$$

Hessian sparsity and structure

Since the main contributions of the Hessian occurs around the diagonal (Chavent and Plessix, 1999; Valenciano and Biondi, 2004), additional computational savings can be obtain by limiting the computation of equation (9) to $\mathbf{y}_T$ points close to $\mathbf{x}_T$. This reduces equation (9) to

$$\mathbf{H}(\mathbf{x}_T, \mathbf{x}_T + \mathbf{a}_\mathbf{x}) = \sum_{\omega} \sum_{\mathbf{x}_s} \mathbf{G}'(\mathbf{x}_T, \mathbf{x}_s; \omega) \mathbf{G}(\mathbf{x}_T + \mathbf{a}_\mathbf{x}, \mathbf{x}_s; \omega) \sum_{\mathbf{x}_r} \mathbf{G}'(\mathbf{x}_T, \mathbf{x}_r; \omega) \mathbf{G}(\mathbf{x}_T + \mathbf{a}_\mathbf{x}, \mathbf{x}_r; \omega), \tag{10}$$

where $\mathbf{a_x} = (a_z, a_x, a_y)$ is the "offset" from the point $\mathbf{x}_T$. Thus only a few elements of the Hessian matrix are computed (non-stationary filter coefficients).

To be able to perform the multidimensional convolution operation in equation (5), the computed Hessian elements in equation (10) have to be placed on a helix (Claerbout, 1998). After that, each row of the Hessian matrix is a multidimensional filter applied to the whole model space.

Chavent and Plessix (1999) qualitatively discuss the amount of the spreading away from the diagonal of the Hessian matrix. Future research will address the optimal number of filter coefficients needed to account for the spreading, since this number has a direct impact on the cost of the method.

NON-STATIONARY LEAST-SQUARES FILTERING

Even though the target-oriented Hessian has a smaller number of rows and columns in equation (9), its condition number could be high, making the solution of the non-stationary least-squares filtering problem in equation (5) unstable. One solution is adding a smoothing regularization operator to equation (5):

$$\begin{aligned} \mathbf{H}\hat{\mathbf{m}} - \mathbf{m}_{mig} &\approx 0, \\ \epsilon \mathbf{I}\hat{\mathbf{m}} &\approx 0, \end{aligned} \tag{11}$$

where the choice of the identity operator (**I**) as regularization operator is arbitrary. Changing the ϵ parameter for such a simple regularization operator is equivalent to stopping the conjugate gradient solver after a different number of iterations.

A more sophisticated regularization scheme could involve applying an smoothing operator in the angle (or ray parameter) dimension (Prucha et al., 2000; Kuehl and Sacchi, 2001). More research need to be done regarding that subject, which is of extreme importance to obtain stable and meaningful results in real case scenarios.

NUMERICAL EXAMPLES

In this section we show two numerical examples of target-oriented Hessians and the corresponding least-squares inverse images. The first example is a constant velocity model and the second is a model with a velocity Gaussian anomaly. The second one was designed to study the effects of uneven illumination due to overburden structure.

Constant-velocity model

Explicitly computing the Hessian is possible when following a target-oriented strategy that exploits the Hessian sparsity and structure. We created a synthetic dataset, using equation

6, with a constant-reflectivity flat reflector (at $z = 0.8\,km$) in a constant-velocity medium ($v = 2.0\,km\,s^{-1}$). Assuming a land acquisition geometry, where the shots and receivers were positioned every $20\,m$ on the interval $\mathbf{x} = [-0.8, 0.8]\,km$. Valenciano and Biondi (2004) discuss in detail the banded nature and sparsity of the Hessian matrix for the constant-velocity model.

Figure 1 shows a 15×15 coefficient filter at constant depth as the x coordinate moves from the corner to the center of the acquisition. Figure 1a shows point 1, with coordinates $\mathbf{x} = (0.8, -0.6)$ (corner of the acquisition). Figure 1b shows point 2, with coordinates $\mathbf{x} = (0.8, -0.4)$. Figure 1c shows point 3, with coordinates $\mathbf{x} = (0.8, -0.2)$. Figure 1d shows point 4, with coordinates $\mathbf{x} = (0.2, 0)$ (at the center of the acquisition).

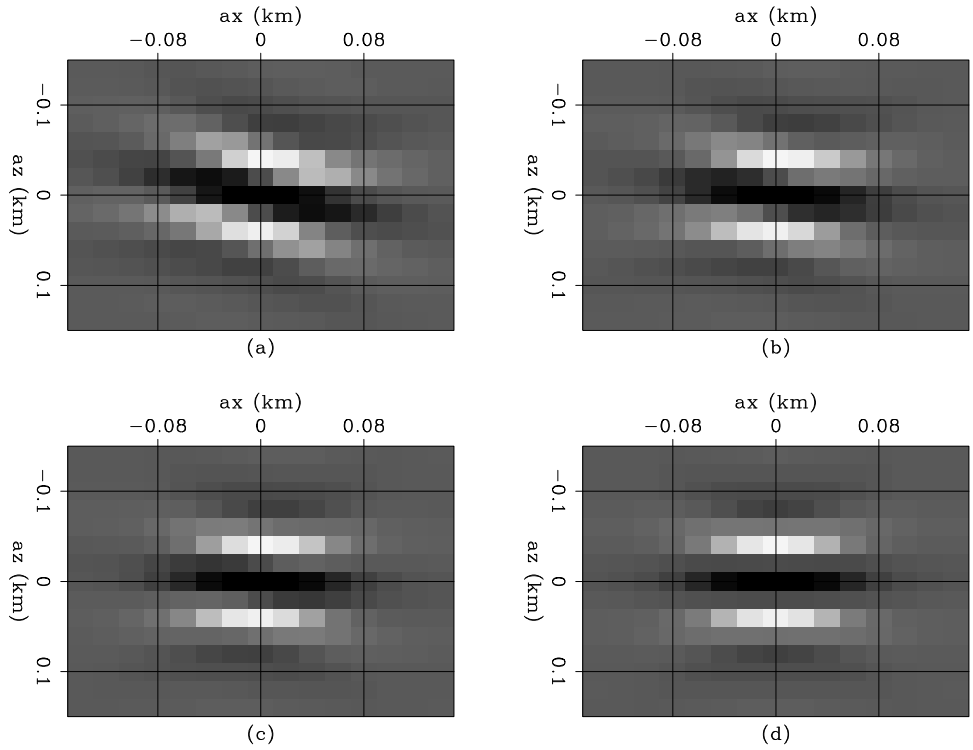

Figure 1: Hessian of the constant-velocity model, (a) point 1 $\mathbf{x} = (0.8, -0.6)$, (b) point 2 $\mathbf{x} = (0.8, -0.4)$, (c) point 3 $\mathbf{x} = (0.8, -0.2)$, and (d) point 4 $\mathbf{x} = (0.2, 0)$. alejandro1-hesian_phase_const [CR]

Figure 2 shows the envelope of the 15×15 coefficient filter shown in Figure 1. The energy of the ellipses become dimer away from the center, indicating that these points have lower illumination due to the acquisition geometry. To correct this effect we computed the least-squares inverse image, by the method described in the above section.

Two different numbers of filter coefficients were used. Figures 3 and 4 show the inversion results for a filter of 11×11 coefficients, whereas Figures 5 and 6 show the inversion results for a filter of 15×15 coefficients. Figure 7 shows a comparison of the best results of both filter sizes.

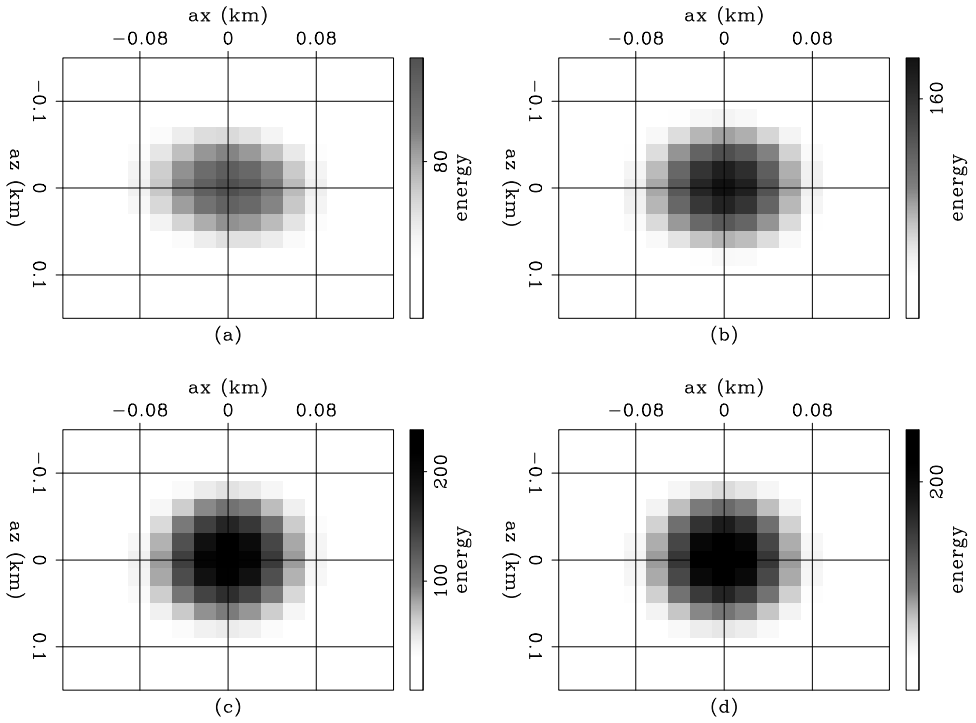

Figure 2: Envelope of the Hessian of the constant-velocity model, (a) point 1 $\mathbf{x} = (0.8, -0.6)$, (b) point 2 $\mathbf{x} = (0.8, -0.4)$, (c) point 3 $\mathbf{x} = (0.8, -0.2)$, and (d) point 4 $\mathbf{x} = (0.2, 0)$. alejandro1-hesian_const [CR]

The panels in Figure 3 show the least-squares inverse image for different numbers of iterations for a filter of 11×11 coefficients: 3a for 10 iterations, 3b for 20 iterations, 3c for 100 iterations, and 3d for migration. Notice how the image amplitudes become more even. Figure 4 shows the comparison of the same least-squares inverse image results at the reflector depth. The image amplitude after 100 iterations is the best result. The conjugate gradient algorithm further balances the image amplitudes, which reduces the effects of the acquisition geometry and the bandlimited characteristic of the seismic data.

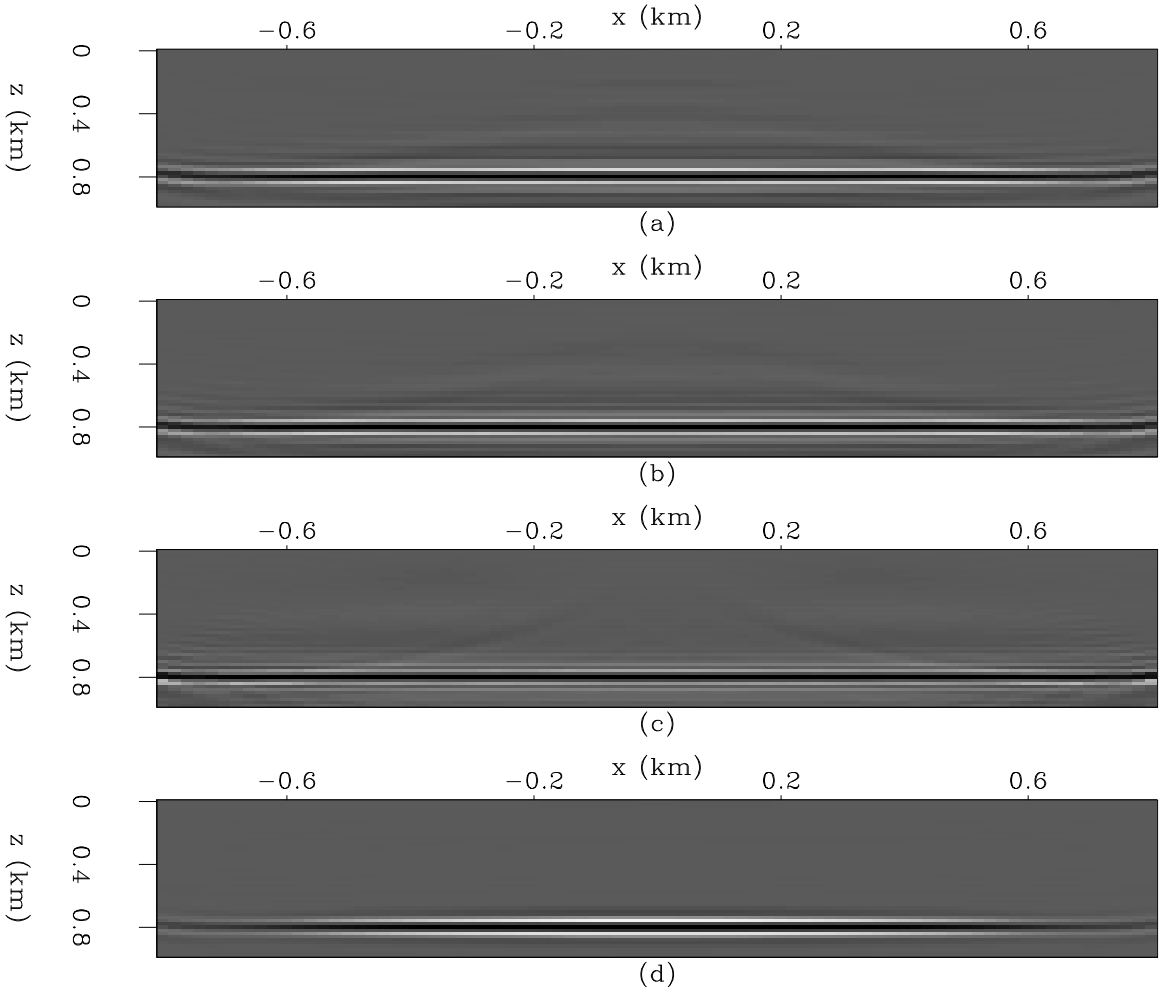

Figure 3: Constant-velocity inversion using a filter size of 11×11 coefficients: (a) 10 iterations, (b) 20 iterations, (c) 100 iterations, and (d) migration. alejandro1-inv_const_11 [CR]

The panels in Figure 5 show the least-squares inverse image for different number of iterations for a filter of 15×15 coefficients: 5a for 10 iterations, 5b for 20 iterations, 5c for 100 iterations, and 5d for migration. Notice again, how the image amplitudes become more even. Figure 6 shows the comparison of the same least-squares inverse image results at the reflector depth. The image amplitude after 100 iterations is the best result. The conjugate gradient algorithm once again further balances the image amplitudes.

Figure 7 compares the migration result to the best inversion results for filter sizes 11×11

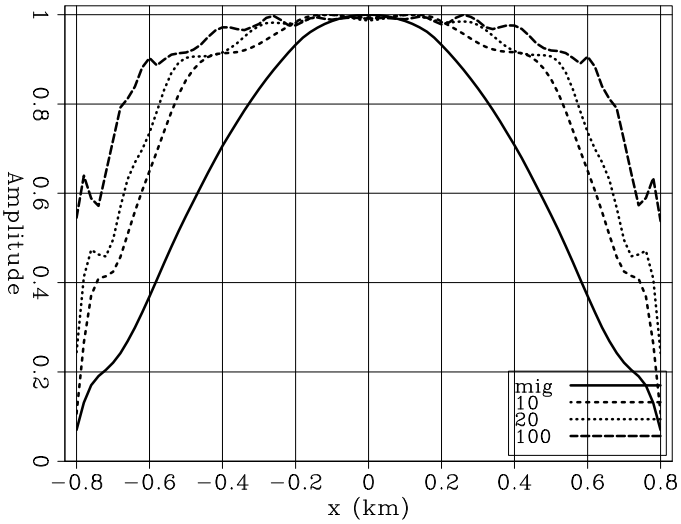

Figure 4: Amplitudes extracted at reflector depth from Figure 3, filter size of 11×11 coefficients. alejandro1-inv_const_pp_11 [CR]

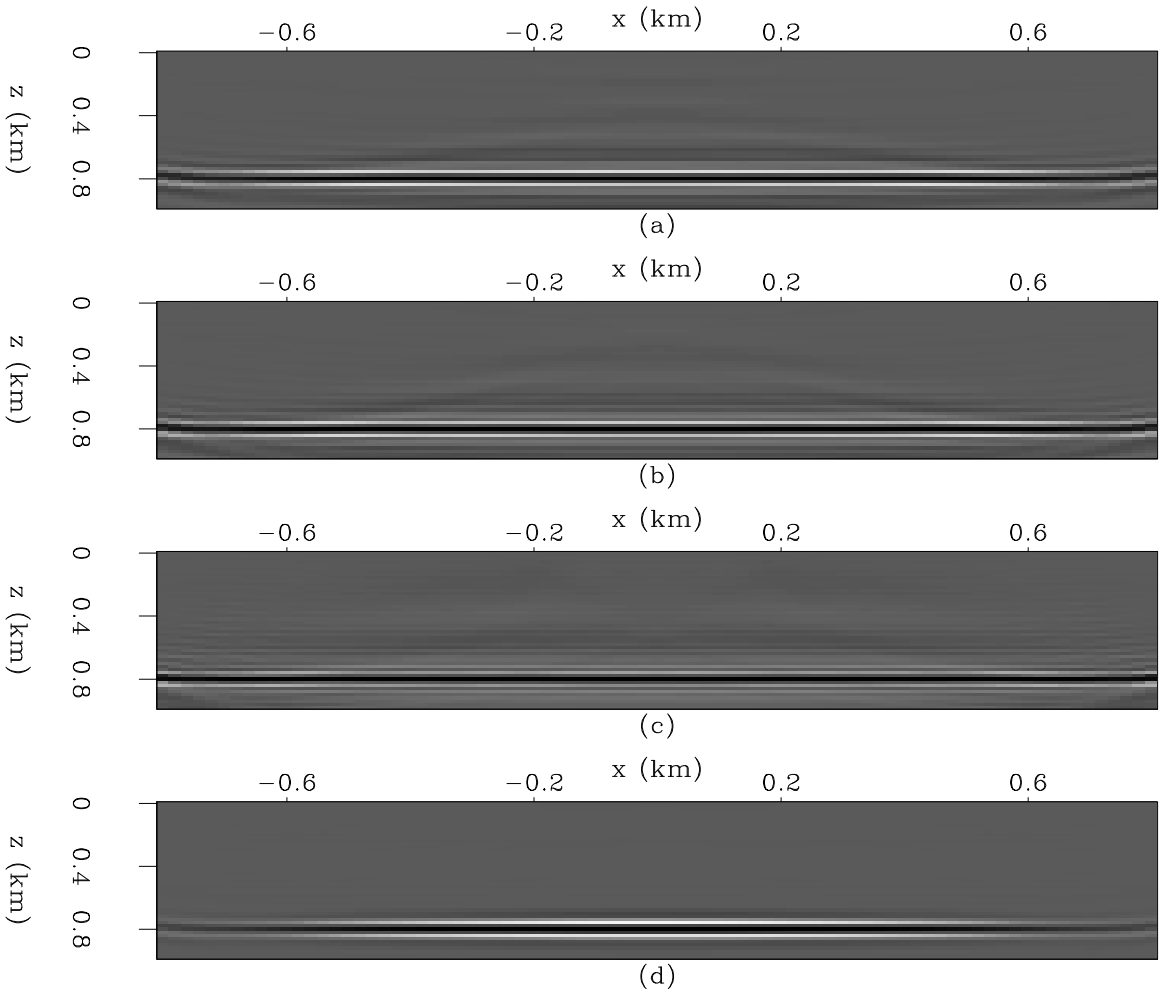

Figure 5: Constant-velocity inversion using a filter size of 15×15 coefficients: (a) 10 iterations, (b) 20 iterations, (c) 100 iterations, and (d) migration. alejandro1-inv_const_15 [CR]

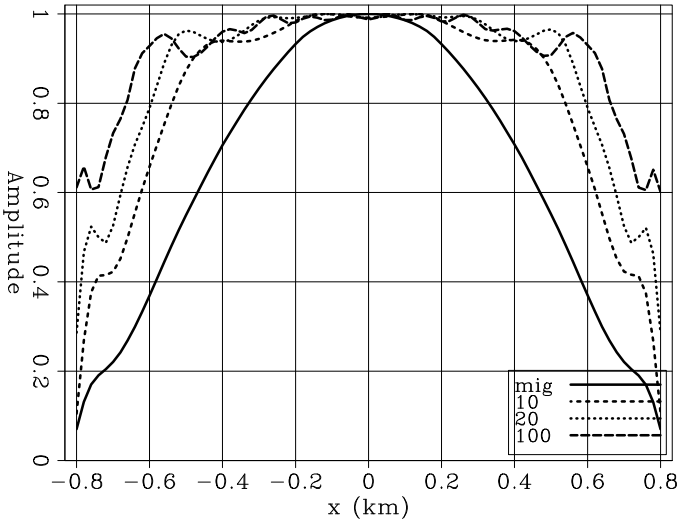

Figure 6: Amplitudes extracted at reflector depth from Figure 5, filter size of 15×15 coefficients. alejandro1-inv_const_pp_15 [CR]

coefficients, 15×15 coefficients. There is not much difference in the recovered amplitudes, thus a filter size of 11×11 should be sufficient.

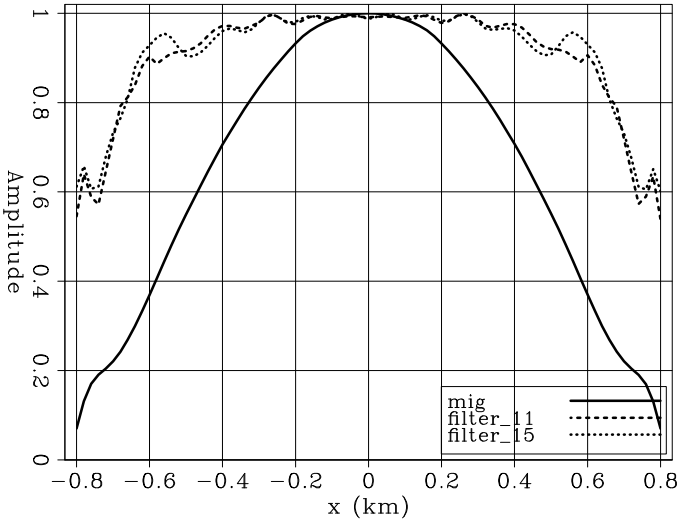

Figure 7: Comparison the migration result to the best inversion results for filter sizes 11×11 coefficients and 15×15 coefficients. alejandro1-inv_const_filter [CR]

Gaussian anomaly velocity model

We created a synthetic dataset, using equation 6, from a model with a constant-reflectivity flat reflector lying beneath a Gaussian low velocity anomaly (Figure 8). Again, we assumed a land acquisition geometry, where the shots and receivers were positioned every 10 m on the interval $\mathbf{x} = [-3.0, 3.0]\ km$.

Figure 9 shows a 15×15 coefficient filter at constant depth as the x coordinate moves from the corner to the center of the acquisition. Figure 9a shows point 1, with coordinates $\mathbf{x} = (2.0, -2.5)$ (corner of the acquisition). Figure 9b shows point 2, with coordinates $\mathbf{x} = (2.0, -1.5)$. Figure 9c shows point 3, with coordinates $\mathbf{x} = (2.0, -0.8)$. Figure 9d shows

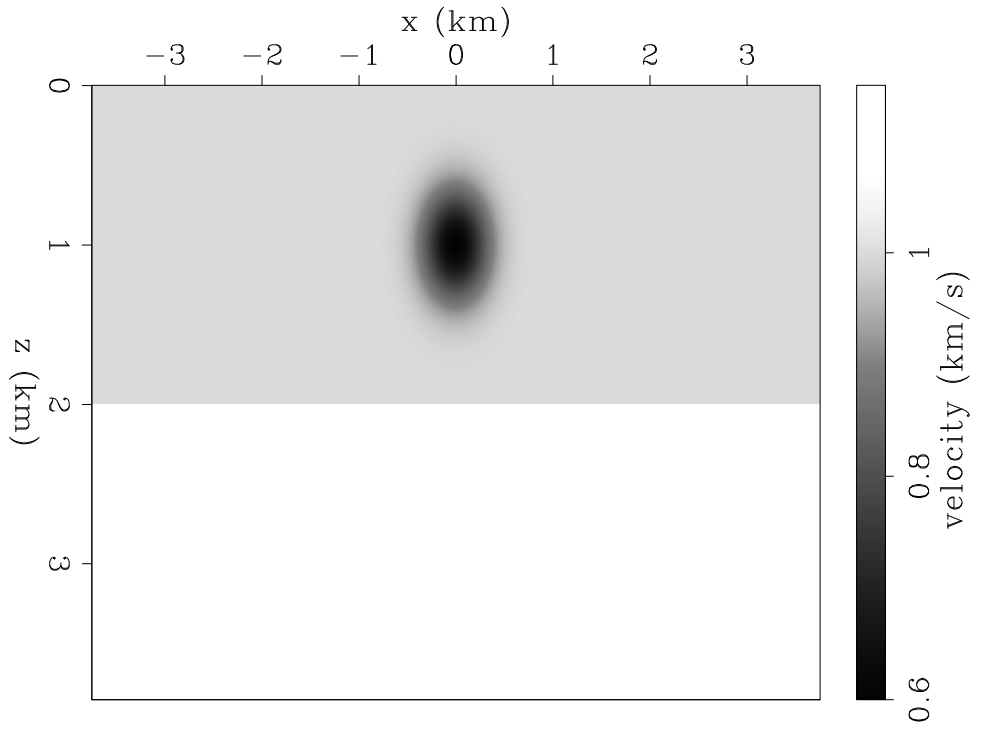

Figure 8: Gaussian anomaly velocity model. alejandro1-bill [ER]

point 4, with coordinates $\mathbf{x} = (2.0, 0.0)$ (at the center of the acquisition). Figure 10 shows the envelope of the 15×15 coefficient filter shown in Figure 9. Differently to the constant velocity case, the higher energy is at point 3 ($\mathbf{x} = (2.0, -0.8)$) (away from the center). This is due to a focusing effect created by the Gaussian velocity anomaly. To correct this effect we computed the least-squares inverse image, by the method described in the above section.

As with the previous example, two different numbers of filter coefficients were used. Figures 11 and 12 show the inversion results for a filter of 11×11 coefficients, whereas Figures 13 and 14 show the inversion results for a filter of 15×15 coefficients. Figure 15 shows a comparison of the best results of both filter sizes.

The panels in Figure 11 show the least-squares inverse image for different number of iterations for a filter of 11×11 coefficients: 11a for 10 iterations, 11b for 20 iterations, 11c for 100 iterations, and 11d for migration. Notice how the image amplitudes become more even, but as the number of iterations increase the result becomes unstable. Figure 12 compares the same least-squares inverse image results at the reflector depth. The image amplitude after 10 iterations is the best result. The conjugate gradient algorithm further balances the image amplitudes, which reduces the effects of acquisition geometry and the bandlimited characteristic of the seismic data. But is not as good reducing the focusing effect (amplitude anomaly at $\mathbf{x} = (2.0, -0.8)$).

The panels in Figure 13 show the least-squares inverse image for different number of iterations for a filter of 15×15 coefficients: 13a for 10 iterations, 13b for 20 iterations, 13c for

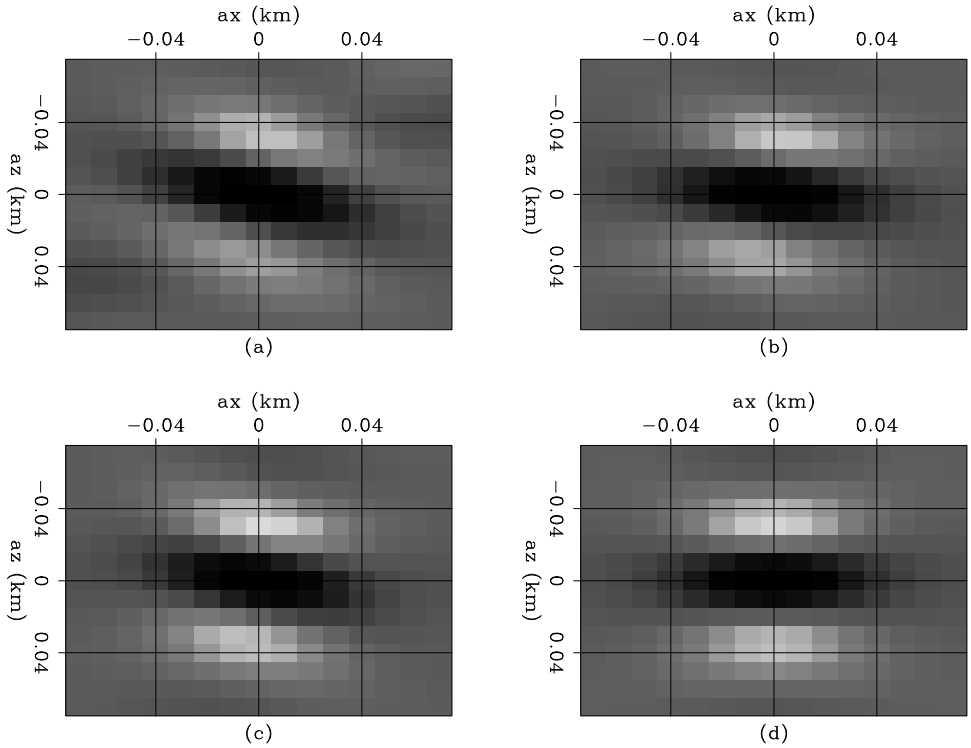

Figure 9: Hessian of the Gaussian anomaly velocity model, (a) point 1 $\mathbf{x} = (2.0, -2.5)$, (b) point 2 $\mathbf{x} = (2.0, -1.5)$, (c) point 3 $\mathbf{x} = (2.0, -0.8)$, and (d) point 4 $\mathbf{x} = (2.0, 0.0)$. alejandro1-hesian_phase_bill_filter [CR]

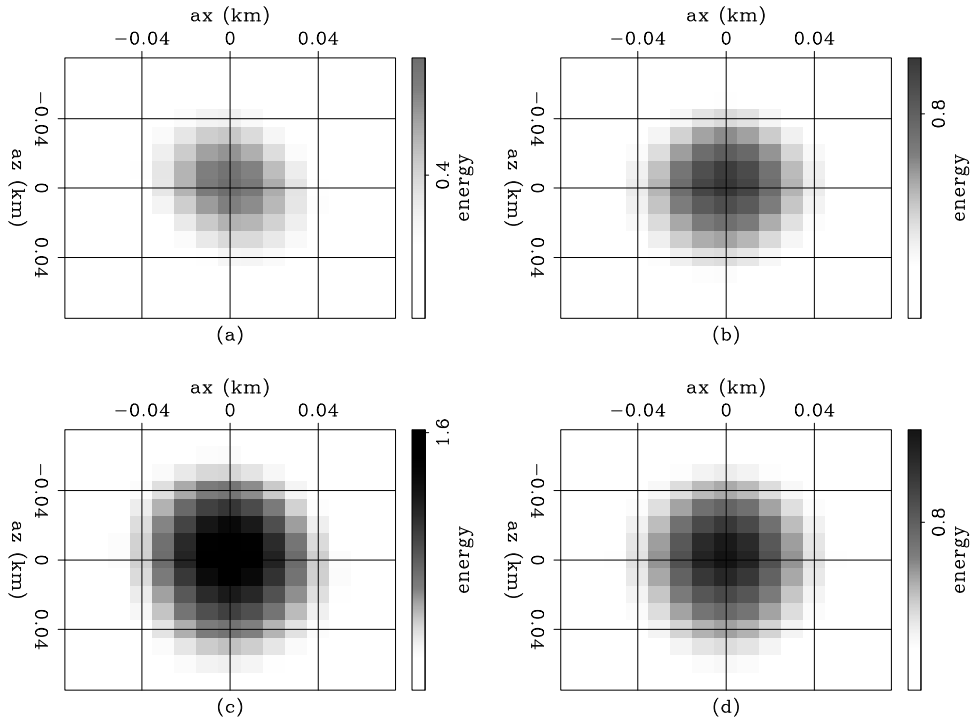

Figure 10: Envelope of the Hessian of the Gaussian anomaly velocity model, (a) point 1 $\mathbf{x} = (2.0, -2.5)$, (b) point 2 $\mathbf{x} = (2.0, -1.5)$, (c) point 3 $\mathbf{x} = (2.0, -0.8)$, and (d) point 4 $\mathbf{x} = (2.0, 0.0)$. alejandro1-hesian_bill_filter [CR]

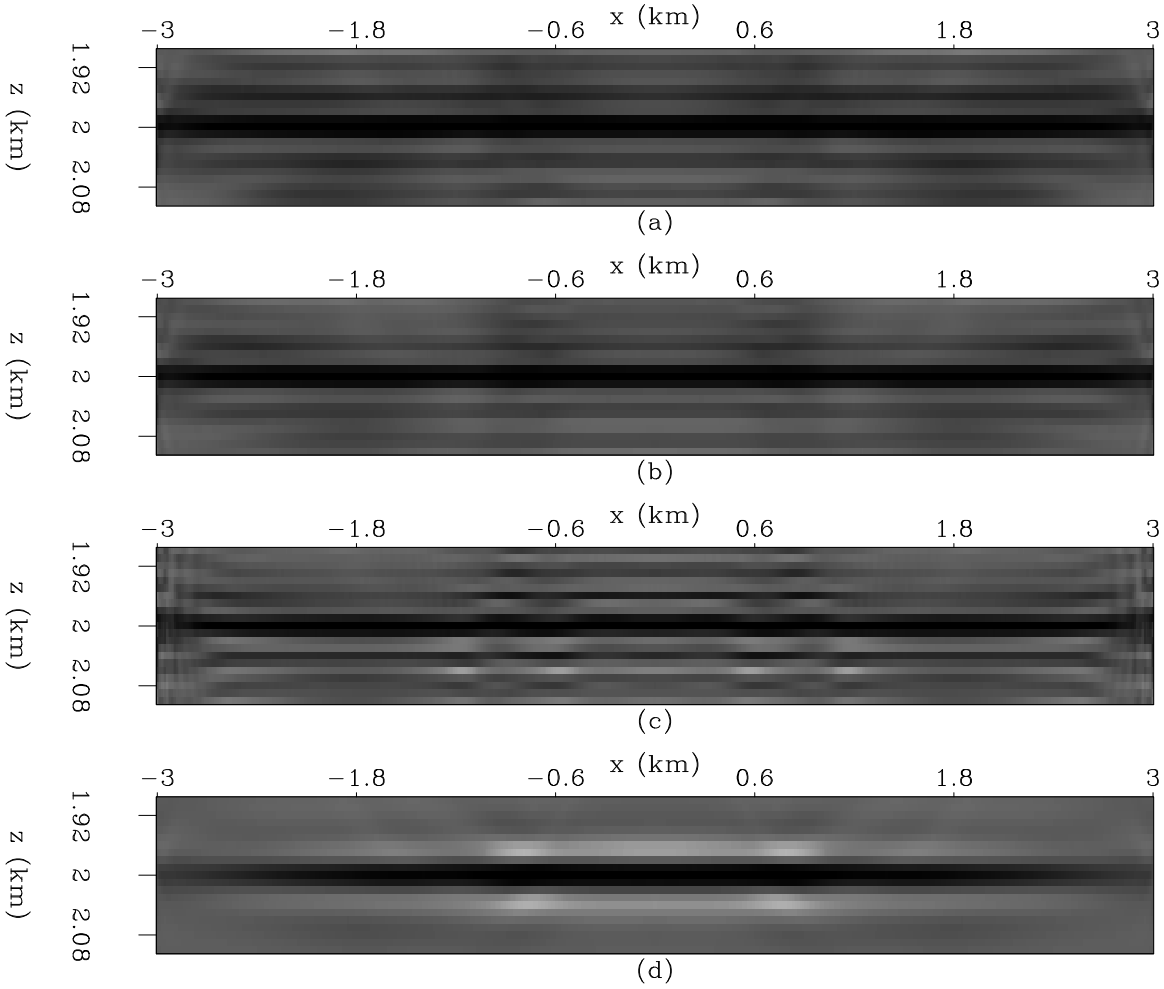

Figure 11: Gaussian anomaly velocity inversion using a filter size of 11×11 coefficients: (a) 10 iterations, (b) 20 iterations, (c) 100 iterations, and (d) migration. alejandro1-inv_bill_11 [CR]

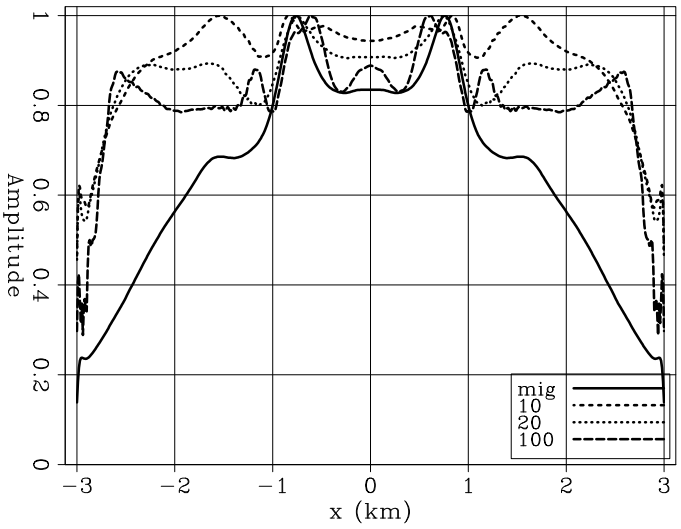

Figure 12: Amplitudes extracted at reflector depth from Figure 11, filter size of 11×11 coefficients. alejandro1-inv_pp_11 [CR]

100 iterations, and 13d for migration. Notice how the image amplitudes become more even, as the number of iterations increase. Figure 14 shows the comparison of the same least-squares inverse image results at the reflector depth. The image amplitude after 100 iterations is the best result. The conjugate gradient algorithm further balances the image amplitudes, reducing the focusing effect as well as the effects of the acquisition geometry and the bandlimited characteristic of the seismic data.

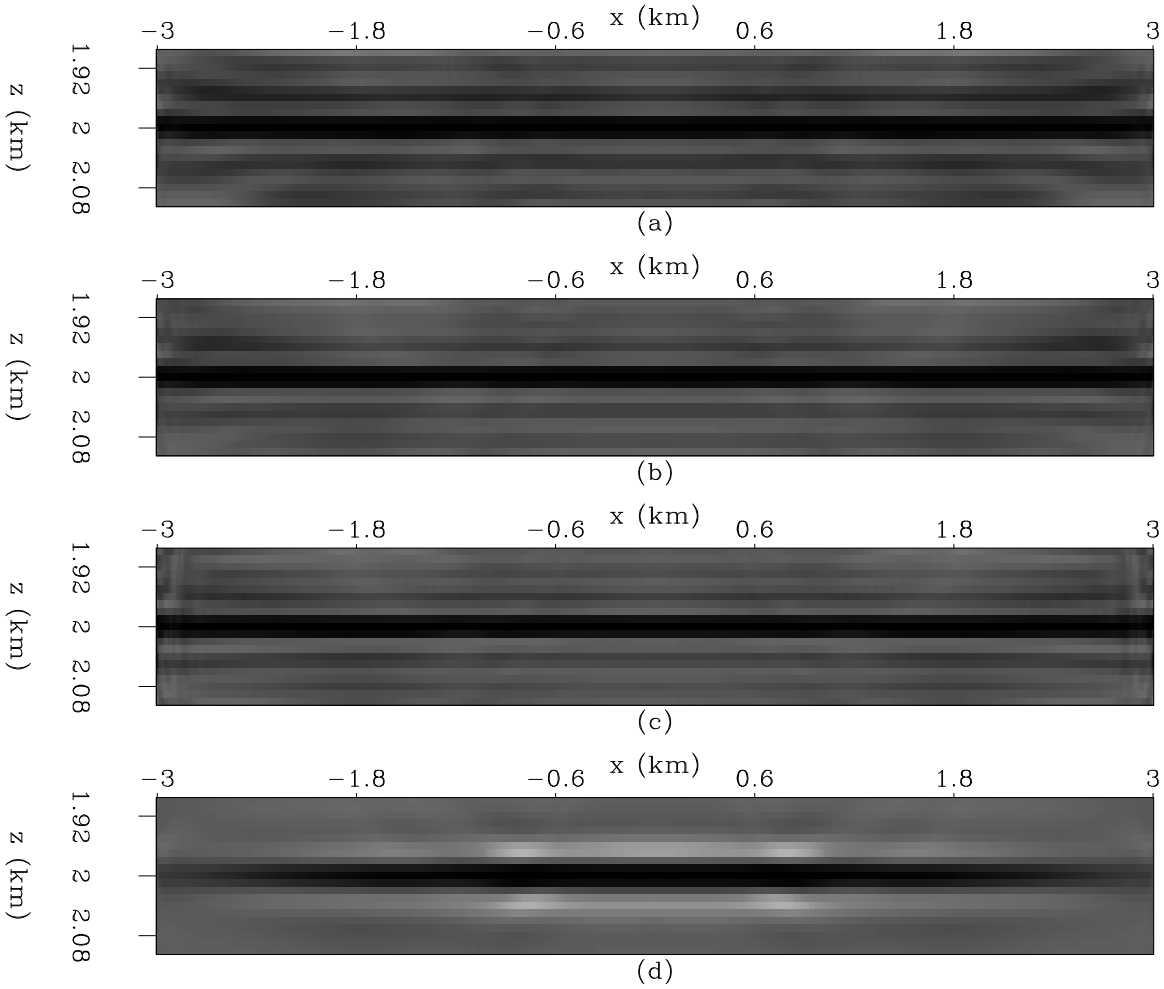

Figure 13: Gaussian anomaly velocity inversion using a filter size of 15×15 coefficients: (a) 10 iterations, (b) 20 iterations, (c) 100 iterations, and (d) migration. alejandro1-inv_bill_15 [CR]

Figure 15 the migration result to the 100 iterations inversion results for filter sizes 11×11 coefficients, 15×15 coefficients. There is a big difference in the recover amplitudes for the different filter sizes being the 15×15 coefficient filter the one that better reduces the effect of the focusing effect on the amplitudes. More research needs to be done to find a way to *a priori* predict the proper filter size.

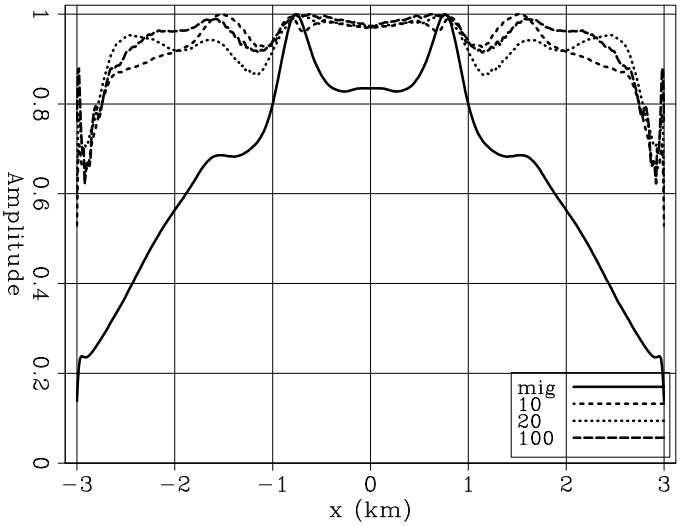

Figure 14: Amplitudes extracted at reflector depth from Figure 13, filter size of 15×15 coefficients. alejandro1-inv_pp_15 [CR]

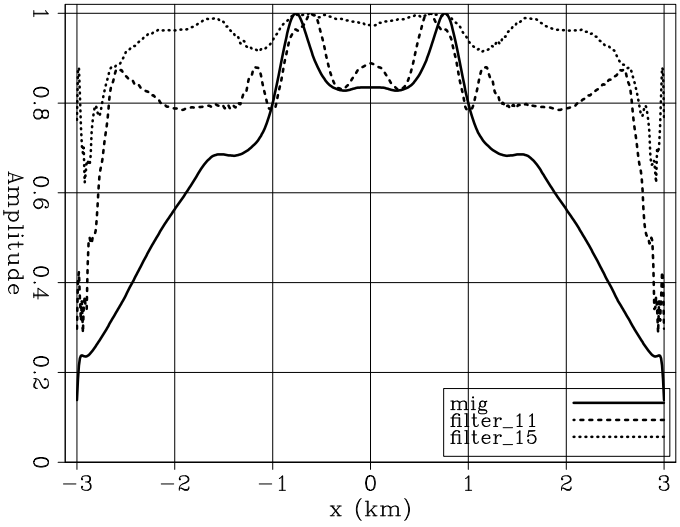

Figure 15: Comparison the migration result to the 100 iterations inversion results for filter sizes 11×11 coefficients and 15×15 coefficients. alejandro1-inv_filter [CR]

CONCLUSIONS

Since accurate imaging of reflections is more important in the neighborhood of the reservoir, a target-oriented strategy can be applied to estimate the wave-equation least-squares inverse image by explicitly computing the Hessian. The main contributions of the Hessian occurs around the diagonal, that is why additional computational savings can be obtain by limiting the its computation to only few elements around it. The least-squares inverse image is then computed as the solution, using a conjugate gradient algorithm, of a non-stationary least-squares filtering problem. This approach allows to perform the number of iterations necessary to achieve the convergence.

Results on the constant velocity model show that the inversion recovers the correct image amplitudes. In this case a filter size of 11×11 is enough to obtain a good result. However, something different happens in the Gaussian anomaly velocity model case, where the inversion gives noisy results if a filter size of 11×11 is used. After adding more coefficients to the filter (filter size of 15×15) a more stable result was obtained.

ACKNOWLEDGMENTS

I would like to thank Bill Symes and TRIP for the Gaussian anomaly velocity model used in this paper.

REFERENCES

Bamberger, A., Engquist, B., Halpern, L., and Joly, P., 1988, Paraxial approximation in heterogeneous media: SIAM J. Appl. Math., **48**, 98–128.

Chavent, G., and Plessix, R. E., 1999, An optimal true-amplitude least-squares prestack depth-migration operator: Geophysics, **64**, no. 2, 508–515.

Claerbout, J. F., 1992, Earth soundings analysis, processing versus inversion: Blackwell Scientific Publications.

Claerbout, J. F., 1998, Multidimensional recursive filters via a helix: Geophysics, **63**, no. 5, 1532–1541.

Duquet, B., and Marfurt, K. J., 1999, Filtering coherent noise during prestack depth migration: Geophysics, **64**, no. 4, 1054–1066.

Ehinger, A., Lailly, P., and Marfurt, K. J., 1996, Green's function implementation of common-offset wave-equation migration: Geophysics, **61**, no. 06, 1813–1821.

Kuehl, H., and Sacchi, M., 2001, Generalized least-squares DSR migration using a common angle imaging condtion: Soc. of Expl. Geophys., 71st Ann. Internat. Mtg, 1025–1028.

Nemeth, T., Wu, C., and Schuster, G. T., 1999, Least-squares migration of incomplete reflection data: Geophysics, **64**, no. 1, 208–221.

Prucha, M. L., Clapp, R. G., and Biondi, B., 2000, Seismic image regularization in the reflection angle domain: SEP–**103**, 109–119.

Ronen, S., and Liner, C. L., 2000, Least-squares DMO and migration: Geophysics, **65**, no. 5, 1364–1371.

Tarantola, A., 1987, Inverse problem theory: Elsevier.

Valenciano, A. A., and Biondi, B., 2004, Target-oriented computation of the wave-equation imaging Hessian: SEP–**117**, 63–76.